Scaling of asymmetric reconnection in compressible plasmas

J. Birn,[1,a)] J. E. Borovsky,[1] M. Hesse,[2] and K. Schindler[3]
[1]*Los Alamos National Laboratory, Los Alamos, New Mexico 87545, USA*
[2]*NASA/Goddard Space Flight Center, Greenbelt, Maryland 20771, USA*
[3]*Ruhr University, D-44780 Bochum, Germany*

(Received 19 February 2010; accepted 23 April 2010; published online 19 May 2010)

The scaling of the reconnection rate with external parameters is reconsidered for antiparallel reconnection in a single-fluid magnetohydrodynamic (MHD) model, allowing for compressibility as well as asymmetry between the plasmas and magnetic fields in the two inflow regions. The results show a modest dependence of the reconnection rate on the plasma beta (ratio of plasma to magnetic pressure) in the inflow regions and demonstrate the importance of the conversion of magnetic energy to enthalpy flux (that is, convected thermal energy) in the outflow regions. The conversion of incoming magnetic to outgoing thermal energy flux remains finite even in the limit of incompressibility, while the scaling of the reconnection rate obtained earlier [P. A. Cassak and M. A. Shay, Phys. Plasmas **14**, 102114 (2007)] is recovered. The assumptions entering the scaling estimates are critically investigated on the basis of two-dimensional resistive MHD simulations, confirming and even strengthening the importance of the enthalpy flux in the outflow from the reconnection site. © *2010 American Institute of Physics*. [doi:10.1063/1.3429676]

I. INTRODUCTION

Magnetic reconnection is generally considered to be the key process in the release of magnetic energy and its conversion to particle kinetic energy in explosive phenomena such as solar flares and magnetospheric substorms. It is also the main mechanism for the transport of magnetic flux, energy, and particles across magnetic boundaries, such as the Earth's magnetopause. Traditional approaches have almost exclusively investigated symmetric reconnection, in which the two plasmas in the inflow regions are identical and differ only by the direction of the reconnecting magnetic field component. However, the more generic case is one in which densities, temperatures, and magnetic field strengths in the two inflow regions are different. This asymmetric reconnection is generally realized at the magnetopause. Asymmetries may also occur in the magnetotail when the two lobes get loaded unevenly,[1] which happens particularly in the presence of a strong east-west magnetic field component,[2] or on the Sun, for instance, when newly emerging magnetic flux interacts with preexisting magnetic loops (e.g., Refs. 3–5).

An important, nontrivial question is how the reconnection rate, measured by the electric field E_r at the reconnection site, scales with the external inflow parameters when they are not identical on the two inflow sides. Reconnection rates in asymmetric configurations have been investigated recently by Cassak and Shay,[6] Borovsky and Hesse,[7] Borovsky *et al.*,[8] and Birn *et al.*,[9] all using resistive MHD. Cassak and Shay[6] used a Sweet–Parker type analysis to derive scaling laws for the reconnection rate (and other parameters) in the incompressible regime for antiparallel reconnection between plasmas of different magnetic field strengths and densities. Their result (converted to MKS units) can be written as

$$E_r = f v_A \bar{B}, \tag{1}$$

where f is a dimensionless factor, typically much smaller than unity, and v_A and $\bar{B}$ represent a hybrid Alfvén speed and a hybrid magnetic field strength, respectively, defined by

$$v_A = \sqrt{\frac{B_1 B_2}{\mu_0 \bar{\rho}}}, \tag{2}$$

$$\bar{B} = \frac{2 B_1 B_2}{B_1 + B_2}, \tag{3}$$

where

$$\bar{\rho} = \frac{B_1 \rho_2 + B_2 \rho_1}{B_1 + B_2}, \tag{4}$$

represents an average density, resulting from the simple mixing of the inflowing plasmas without compression. Subscripts 1 and 2 denote the quantities in the two inflow regions. In the incompressible model of Ref. 6, $\bar{\rho}$ also represents an estimate for the density in the outflow region.

In symmetric configurations, $\bar{B}$ is the magnetic field strength and v_A the Alfvén speed in either inflow region. In such scenarios frequently the dimensionless factor f, equivalent to the Alfvén Mach number in the inflow region, is denoted the reconnection rate. In classical resistive magnetohydrodynamic (MHD) models of reconnection the magnitude of f is controlled by the magnitude of the resistivity η. For instance, in the steady-state Sweet–Parker model[10,11] f is proportional to $\eta^{1/2}$, whereas Petschek's model of fast reconnection[12,13] permits a much higher reconnection rate, which depends only weakly (logarithmically) on the resistivity and may reach $f \approx 0.1$. Similar rates are also found in simulations of collisionless reconnection, in which Hall effects and ion particle dynamics become important (e.g., Refs. 14 and 15).

a)Electronic mail: jbirn@lanl.gov.

The Cassak–Shay scaling (1) was tested and approximately verified in various resistive MHD simulations of reconnection: for the special case of initially uniform density,[6] for cases with identical magnetic field strengths but different densities,[7] in driven and nondriven scenarios in which both B and ρ differed in the two inflow regions,[9] as well as in Hall-MHD simulations,[16] all based on initially one-dimensional plane current sheets without guide field (the magnetic field component in the current direction), and in global magnetospheric MHD simulations.[8] Despite the fact that these simulations included compressibility, reasonable agreement with the Cassak–Shay formula (1) was found, which is based on incompressibility and does not include a dependence on the plasma beta (ratio of plasma over magnetic pressure).

The influence of the plasma beta was investigated in observations by Paschmann *et al.*,[17] which indicated that the occurrence rate of fast flows at the magnetopause was reduced for increasing beta, presumably reflecting lower effectiveness of collisionless reconnection or tearing instability. In contrast, a study by Gosling *et al.*[2] did not show a significant influence of beta. A possible reason is that this study included much stronger guide fields, which are expected to lower compressibility. A theoretical study of collisionless tearing instability by Ding *et al.*[18] confirmed a strong stabilization with increasing beta for the symmetric case but showed only little effect of the magnetosheath beta in an asymmetric case without guide field. Using particle-in-cell (PIC) simulations, Pritchett[19] found a reduction of the reconnection rate for asymmetric cases by factors of 2–3 compared to similar symmetric case but did not investigate the role of beta.

We will again address the reconnection problem from the one-fluid MHD approach, allowing for compressibility in addition to asymmetry. Although for many space scenarios a kinetic approach seems more appropriate, the fluid limit seems sufficient to explore the dependence of the reconnection rate on the external parameters. In Sec. II, we reconsider the scaling of the reconnection rate and the energy conversion based on an integral approach similar to that outlined by Priest and Forbes[20] for the symmetric case and by Cassak and Shay[6] for the asymmetric incompressible case. In Secs. III and IV, we will then check the scaling and the energy conversion estimates, respectively, on the basis of resistive MHD simulations in different asymmetric configurations. This is followed by a summary and discussion in Sec. V.

II. SCALING

A. General asymmetric case

The basic scenario is illustrated in Fig. 1, using notations consistent with Refs. 12 and 6. Inflow parameters are denoted with subscripts 1 and 2, respectively, and outflow parameters with the subscript "o." Consistent with previous approaches we consider a steady state, i.e., $\partial/\partial t \equiv 0$. The conservation of inflow and outflow quantities are obtained from integrating over the surface of a box with a width of 2δ and a length of $2L$ (dashed rectangle), assuming $\delta/L=\epsilon \ll 1$. Here, we are not concerned with a full solution inside and/or outside the box but rather with the scaling obtained from

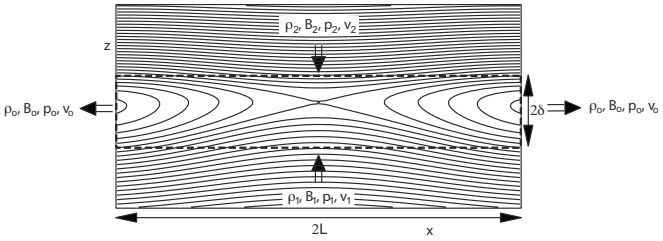

FIG. 1. Schematic of the reconnection site for asymmetric reconnection.

simple balance arguments, analogous to the approach by Ref. 6. In this approach variations of the inflow parameters over the length of the box are neglected. We identify B_1 and B_2 as the absolute values of the x components and consider the B_z components in the inflow regions as small of order ϵ. Similarly, v_1 and v_2 are the absolute values of the z components of the inflow velocity and the v_x components are considered small of order ϵ. In the present paper we also neglect the magnetic field component B_y, often denoted as "guide field." This component will be included in a follow-up paper.

Mass conservation in the box of Fig. 1 gives

$$L(\rho_1 v_1 + \rho_2 v_2) = 2\delta \rho_o v_o. \tag{5}$$

The assumption of steady state with Faraday's law implies that the electric field in the y direction, out of the plane of Fig. 1, is uniform, defining the reconnection rate

$$E_r = v_1 B_1 = v_2 B_2 = v_o B_o. \tag{6}$$

Equations (5) and (6) are consistent with the approaches by Cassak and Shay[6] and Swisdak and Drake.[21] We note that $v_o \approx v_{ox}$ and $B_o \approx B_{oz}$ if the outflow is primarily in the x direction.

Next we consider force balance, starting with the z direction. It is easy to see that the inertia terms in the inflow regions are of order ϵ^2 and thus negligible. This leads to the pressure balance

$$p_1 + \frac{B_1^2}{2\mu_0} = p_2 + \frac{B_2^2}{2\mu_0} = p_{\rm tot}. \tag{7}$$

Furthermore, this pressure balance must also hold approximately at the outflow locations $x=\pm L$, because the inflow parameters, including $p_{\rm tot}$, are assumed to be approximately constant over the scale length L, that is

$$p_o + \frac{B_{ox}^2 + B_{oz}^2}{2\mu_0} \approx p_{\rm tot}. \tag{8}$$

Considering our scaling $\epsilon=\delta/L \ll 1$, we find that v_1 and v_2, and consequently $\mathbf{B}_o$ should be of order ϵ. It seems therefore justified in lowest order to neglect the magnetic pressure as being of order ϵ^2 in the outflow region, such that

$$p_o \approx p_{\rm tot}, \tag{9}$$

which is also the pressure at the x-point.

Now we consider force balance in x

$$\rho \mathbf{v} \cdot \nabla v_x = -\partial p/\partial x + j_y B_z. \tag{10}$$

In the classical approaches of Sweet[10] and Parker[11] for symmetric reconnection the outflow pressure p_o is equated to the inflow pressure $p_i = p_1 = p_2$ and the acceleration is assumed to result from the pressure difference between the x-point and the outflow region. This is equivalent to neglecting the Lorentz force term in Eq. (10). If $\rho \mathbf{v} \cdot \nabla v_x$ is approximated by $\rho v_x \partial v_x/\partial x = (\rho/2)\partial v_x^2/\partial x$ and ρ is assumed constant, Eq. (10) then yields

$$p + \rho v_x^2/2 = \text{const}. \tag{11}$$

Using the pressure balance (7) at the location of the x-point then leads to

$$v_o = v_A = B_i/\sqrt{\mu_0 \rho_i}. \tag{12}$$

However, our pressure balance arguments above show that the assumption $p_o \approx p_i$ is not consistent with pressure balance in z and that it is more appropriate in the stretched geometry of Fig. 1 to neglect the pressure gradient in Eq. (10). This is consistent with the approaches taken by Petschek,[12] Soward and Priest,[22] Priest and Forbes[20] (reconsidering the Sweet–Parker model) for symmetric configurations, and by Swisdak and Drake[21] for asymmetric configurations. Consistent with the latter, we approximate

$$\rho \mathbf{v} \cdot \nabla v_x \approx \rho_o v_o^2/L, \tag{13}$$

and

$$|j_y B_z| \approx \frac{B_1 + B_2}{2\mu_0 \delta} B_o. \tag{14}$$

Equating Eqs. (13) and (14) and using Eqs. (5) and (6) lead to

$$v_o^2 = \frac{B_1 B_2}{\mu_0 \bar{\rho}}, \tag{15}$$

where $\bar{\rho}$ is defined by Eq. (4). (A different form of derivation, based on integral momentum conservation, is considered in the Appendix.) This is identical to the results of Swisdak and Drake[21] and Cassak and Shay;[6] however, in the latter, v_o was obtained from energy balance arguments rather than force balance. The result (15), when specified for the symmetric compressible case, is identical to the outflow speed obtained for the incompressible case and with Eq. (2.16) of Soward and Priest[22] for compressible cases. However, it differs from Eq. (4.47) of Priest and Forbes,[20] in which the inflow density is replaced by the outflow density. This difference may have resulted from estimating $B_o/\delta \approx B_i/L$ on the basis of $\nabla \cdot \mathbf{B} = 0$, rather than the combination of Eqs. (5) and (6), which yields $B_o/(\rho_o \delta) \approx B_i/(\rho_i L)$. We note here again that, to the lowest order in δ/L, B_i is assumed to be constant over the scale length L, such that L and δ are not necessarily the scales defined by $\nabla \cdot \mathbf{B} = 0$.

Using Eq. (15) together with Eqs. (5) and (6), we now obtain the reconnection rate

$$E_r = \frac{\delta}{L} v_o \bar{B} \frac{\rho_o}{\bar{\rho}}, \tag{16}$$

where v_o is given by Eq. (15) and $\bar{B}$ is defined by Eq. (3). Equation (16) is identical to the Cassak–Shay result, except for the compression factor $r \equiv \rho_o/\bar{\rho}$.

To estimate the compression factor r, we now use the energy flux balance, including three forms of energy flux

$$\mathbf{S} = \mathbf{E} \times \mathbf{B}/\mu_0 \quad \text{(Poynting flux)}, \tag{17}$$

$$\mathbf{H} = (u + p)\mathbf{v} = \frac{\gamma}{\gamma - 1} p \mathbf{v} \quad \text{(enthalpy flux)}, \tag{18}$$

$$\mathbf{K} = (\rho v^2/2)\mathbf{v} \quad \text{(bulk kinetic energy flux)}. \tag{19}$$

Here $u = p/(\gamma - 1)$ is thermal energy density; for $\gamma = 5/3$ and $p = nkT$, $u = 3nkT/2$. We note that the Poynting vector (17) does not simply represent convected magnetic energy but includes in addition the energy flux resulting from the work done by the (magnetic part of) Maxwell's stress tensor. This is analogous to the enthalpy flux (18), which also, in addition to convected thermal energy ($u\mathbf{v}$), includes the work done by the plasma pressure ($p\mathbf{v}$, or more generally, $\underline{\mathbf{P}} \cdot \mathbf{v}$).

Consistent with previous approximations we neglect bulk kinetic energy in the inflow region and Poynting flux in the outflow region and obtain

$$\left[\left(\frac{B_1^2}{\mu_0} + \frac{\gamma}{\gamma - 1} p_1\right) v_1 + \left(\frac{B_2^2}{\mu_0} + \frac{\gamma}{\gamma - 1} p_2\right) v_2\right] L = \left(\frac{\gamma}{\gamma - 1} p_o + \frac{1}{2} \rho_o v_o^2\right) 2\delta v_o. \tag{20}$$

Equation (20) differs from the result of Cassak and Shay[6] in that enthalpy flux H is included in both inflow and outflow and that the magnetic energy flux in the inflow regions is given by $(B^2/\mu_0)v$. After some algebra and using Eqs. (5)–(7), (9), and (15), one finds

$$r \equiv \frac{\rho_o}{\bar{\rho}} = \frac{\Gamma(B_1 + B_2)}{\lambda_1 B_2 + \lambda_2 B_1}, \tag{21}$$

where

$$\Gamma = \gamma/(\gamma - 1), \tag{22}$$

$$\lambda_i = (1 + \Gamma \beta_i)/(1 + \beta_i), \quad i = 1,2, \tag{23}$$

$$\beta_i = 2\mu_0 p_i/B_i^2, \quad i = 1,2. \tag{24}$$

After insertion of expressions (3), (4), (15), and (28) into Eq. (16), the reconnection rate is given by

$$E_r = \frac{2\delta}{L} \frac{B_1^{3/2} B_2^{3/2}}{\sqrt{\mu_0(\rho_2 B_1 + \rho_1 B_2)(B_1 + B_2)}} \frac{\Gamma(B_1 + B_2)}{\lambda_1 B_2 + \lambda_2 B_1}. \tag{25}$$

Expression (25) includes the effects of compressibility and enthalpy flux.

The incompressible limit of the reconnection rate (25) can be obtained either for $\gamma \to \infty$ (corresponding to $\Gamma \to 1$ and $\lambda_i \to 1$) or for $\beta_i \to \infty$ (corresponding to $\lambda_i \to \Gamma$). In either case, $\rho_o \to \bar{\rho}$ and we recapture the Cassak–Shay result for the

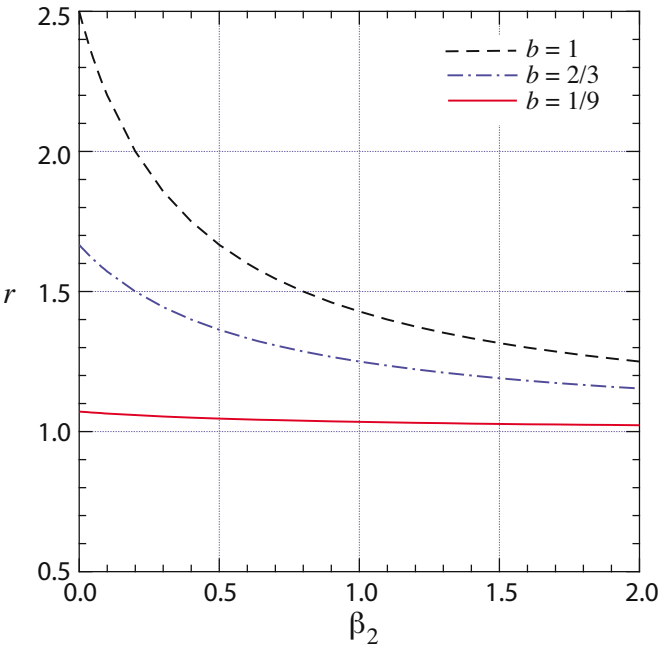

FIG. 2. (Color online) Compression factor $r=\rho_o/\bar{\rho}$ of the reconnection rate as function of the plasma beta in the high-field inflow region, β_2, for $\gamma=5/3$ and various magnetic field ratios $b=B_1/B_2$.

reconnection rate. Note, in contrast, that the energy fluxes also include finite enthalpy flux, which reduces to $p\mathbf{v}$ in the incompressible limit $\gamma\to\infty$.

The expression for r can be further simplified if we normalize the magnetic fields to B_2, assumed to be the larger one, defining

$$b = B_1/B_2. \tag{26}$$

The pressure balance (7) relates β_1 and β_2 with b via

$$b^2(1+\beta_1) = 1+\beta_2. \tag{27}$$

This yields

$$r = \frac{\Gamma(1+\beta_2)}{\Gamma(1+\beta_2)-(\Gamma-1)b}. \tag{28}$$

The compression factor $r=\rho_o/\bar{\rho}$ is shown in Fig. 2 as function of the plasma beta in the high-field inflow region, β_2, for $\gamma=5/3$ and various magnetic field ratios $b=B_1/B_2$. When the ratio between B_2 and B_1 is large ($b\to 0$) we find $r=1$, that is, the incompressible limit. This results from the fact that for small b the plasma beta must be large on the low-field side to ensure pressure balance.

B. Energy conversion and transfer

We can now also compare the different in- and outgoing energy fluxes (17)–(19), integrated over the lengths $2L$ or 2δ, respectively. The result becomes particularly simple, if the fluxes are normalized by the total incoming Poynting flux, which is given by $S_{in}L=(S_1+S_2)L$ for a half box. We find

$$\tilde{S}_1 = \frac{b}{1+b}, \tag{29}$$

$$\tilde{S}_2 = \frac{1}{1+b}, \tag{30}$$

$$\tilde{H}_1 = \frac{\Gamma b\beta_1}{2(1+b)}, \tag{31}$$

$$\tilde{H}_2 = \frac{\Gamma\beta_2}{2(1+b)}, \tag{32}$$

$$\tilde{H}_o = \frac{1}{2} + \Gamma\frac{b\beta_1+\beta_2}{2(1+b)}, \tag{33}$$

$$\tilde{K}_o = \frac{1}{2}, \tag{34}$$

where the symbol $\tilde{}$ denotes the integrated normalized quantities. This shows that 1/2 of the incoming Poynting flux gets converted to bulk kinetic energy flux, as found earlier for the symmetric Sweet–Parker model (e.g., Ref. 20). Subtracting Eqs. (31) and (32) from Eq. (33) shows that the remaining half is converted to enthalpy flux. This result is found independent of the values of γ, β, densities, and the magnetic field ratio b. It will be evaluated critically in Sec. IV on the basis of numerical simulations.

C. Symmetric case

For the symmetric case we obtain

$$r = \frac{\Gamma(1+\beta_i)}{1+\Gamma\beta_i}. \tag{35}$$

We may now interpret the subscript i as representing "inflow." This result is consistent with Eq. (2.18) obtained by Soward and Priest.[22] It is equal to the compression factor obtained for switch-off shocks in the limit of small B_n and v_n, where the subscript n denotes the components normal to the shock. We note, however, that our derivation does not require the presence of shocks. The factor r varies between Γ (=2.5 for $\gamma=5/3$) for $\beta_i\to 0$ and 1 for large β, as shown in Fig. 2 (dashed line).

The energy fluxes in the outflow region are given by

$$H_o = \Gamma p_o v_o = \Gamma\frac{B_i^2}{2\mu_0}(1+\beta_i)v_o, \tag{36}$$

and

$$K_o = \frac{1}{2}\rho_o v_o^2 v_o = r\frac{B_i^2}{2\mu_0}v_o. \tag{37}$$

Because of $r\le\Gamma$, the bulk kinetic energy flux is generally smaller than the total enthalpy flux, which includes a transmitted portion in addition to the converted part; the two fluxes become equal for $\beta_i\to 0$.

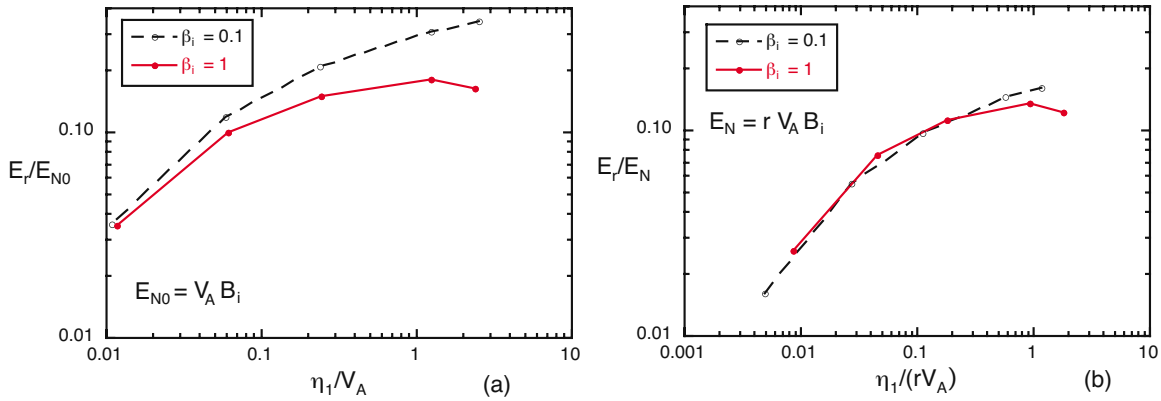

FIG. 3. (Color online) Maximum reconnection rates as function of resistivity for symmetric reconnection with two values of β in the inflow region. (a) Normalized based on the Cassak–Shay formula for the incompressible limit and (b) scaled by including the compression factor r given by Eq. (28).

D. Fast reconnection and Sweet–Parker regime

Our formulas for the reconnection rate (16) or Eq. (25) still contain the undetermined factor δ/L. The magnitude of this factor depends on the physics of the dissipation region and its surroundings including the boundary conditions. Here we will consider only two limits. Simulations of fast collisionless reconnection (e.g., Ref. 14), as well as resistive MHD simulations in the regime of large but localized resistivity (e.g., Refs. 8, 16, 23, and 24; see also Sec. III), indicate that there is a rough maximum value of the order of 0.1, which depends only weakly, if at all, on the dissipation mechanism. Sometimes this regime of fast reconnection is denoted Petschek reconnection. We note, however, that the magnetic structure in this regime does not necessarily include slow shocks (particularly in collisionless reconnection), which are a characteristic of the Petschek model, and that the distinction between "fast" Petschek and "slow" Sweet–Parker reconnection in resistive MHD is not meaningful for large resistivity when the Lundquist number (frequently called magnetic Reynolds number)

$$R_m = \mu_0 L V_A/\eta, \tag{38}$$

approaches unity.

For small resistivity (large Lundquist number), the Sweet–Parker limit can be derived when the current layer thickness 2δ is identified with the width of the diffusion region.[6] The scaling follows from equating the reconnection electric field with the ohmic dissipation term at the x-line

$$E_r = v_o B_o = \eta J \approx \eta \frac{B_1 + B_2}{2\mu_0 \delta}. \tag{39}$$

Using Eqs. (5) and (6), one then obtains

$$f = \frac{\delta}{L} r \sim \sqrt{r \frac{\eta}{\mu_0 L v_o} \frac{B_1 + B_2}{\bar{B}}}, \tag{40}$$

and

$$E_r \sim \sqrt{r \frac{\eta v_o}{\mu_0 L} B_1 B_2}. \tag{41}$$

The expression for E_r is identical to Eq. (34) of Ref. 6, except for the factor $\sqrt{r}$ (and the use of the MKS system).

III. MHD SIMULATION RESULTS: SCALING OF THE RECONNECTION RATE

In the following we will use resistive MHD simulations as described in Ref. 9 to check the reconnection rates for the modified scaling in the context of temporally and spatially varying fields. In Sec. IV, we then investigate the energy conversion and the validity of the simplified scaling assumptions. The initial configurations consist of one-dimensional plane current sheets with shifted Harris-type magnetic field profiles given by

$$B_x = [\tanh(z-a) + a]/(1+a). \tag{42}$$

The initial normalization is such that $\rho_1 = 1$ and $B_2 = 1$ far away from the current sheet. Reconnection is initiated by imposing spatially localized resistivity given by

$$\eta = \eta_1/\cosh^2 s \quad s^2 = x^2/d_x^2 + (z-z_0)^2/d_z^2. \tag{43}$$

The resistivity is centered at the (varying) location of the magnetic null (x-point) z_0, where $B_x = 0$ and $B_z = 0$. The normalized maximum resistivity η_1 corresponds to the inverse of the Lundquist number (38), based on the half-width of the unperturbed current sheet as characteristic length.

Two scenarios are considered, distinguished as "driven" and "nondriven." The driven scenario is based on the "Newton challenge" problem,[15] which consists of magnetic reconnection forced by compression through temporally and spatially localized inflow into the exterior regions of a relatively small box with half-lengths $L_x = 8$ and $L_z = 4$ For the nondriven problem, without inflow, a much larger box size is chosen to reduce the effects of boundary stabilization, $L_x = 100$ and $L_z = 40$.

The reconnection rate in the resistive regime depends not only on the external parameters in the inflow regions but also on the magnitude of resistivity. Therefore, as in Ref. 9, we consider the scaling together with the resistivity dependence,

TABLE I. Initial parameters for four asymmetric cases.

Case	B_1/B_2	ρ_2/ρ_1	v_{A1}	v_{A2}	β_1	β_2
A	1/9	0.4	0.111	1.581	96	0.2
B	1/9	10	0.111	0.316	96	0.2
C	2/3	0.4	0.667	1.581	1.68	0.2
D	2/3	10	0.667	0.316	1.68	0.2

trying to match curves rather than single points. Figure 3 shows the maximum reconnection rates as function of resistivity for two values of β in the inflow region in symmetric nondriven cases. The scale size for the resistivity was chosen as $d_x=d_z=0.5$. The results in Fig. 3(a) are scaled based on the Cassak–Shay formula for the incompressible limit while the reconnection rates in Fig. 3(b) are scaled by including the compression factor r given by Eq. (28). The normalized resistivity on the abscissa corresponds to the inverse of the Lundquist number R_m defined by Eq. (38), using the half-thickness $L_z=1$ of the unperturbed current sheet as a characteristic scale length. As discussed in Sec. II D, the resistivity dependence of the scaling factor f at low resistivity also includes a dependence on the compression ratio r, as given in Eq. (40). This dependence is therefore included in the abscissa values of Fig. 3(b). However, it is not clear, whether this scaling is also appropriate at larger resistivities, when the Lundquist number (38) becomes comparable to, or even smaller than unity. Inclusion of the compression factor improves the matching considerably. Figure 3 also demonstrates the transition from the slow Sweet–Parker regime at small η (with E_r approximately proportional to $\eta^{1/2}$) to a fast ("Petschek") regime at large η, where the reconnection rate approaches a maximum of ~0.1 (in normalized units) and the dependence on η weakens.

Next we reconsider the scaling of four cases with various density and magnetic field ratios discussed by Birn *et al.*[9] defined in Table I. Figure 4 shows the maximum reconnection rates as function of resistivity for (left) driven and (right) nondriven cases. The scaling in the top panels is based on the Cassak–Shay formula for the incompressible limit, while the reconnection rates in the bottom panels are rescaled by including the compression factor r given by Eq. (28). Inclusion of the compressibility improves the matching particularly for the nondriven cases (right panels). To obtain a quantitative measure of the improvement we fitted the logarithmic values of Fig. 4 to single second-order polynomials and calculated the average deviations of the reconnection rates from these curves. We found that including the compression factor reduced the average deviation from 8.2% to 7.0% in the driven cases and from 10.1% to 6.5% in the nondriven cases. The lack of a significant improvement in the driven cases is related to the fact that the compression factor r given by Eq. (28) does not include a density dependence. Therefore the relative differences between cases A and B and between cases C and D, respectively, which each belong to the same

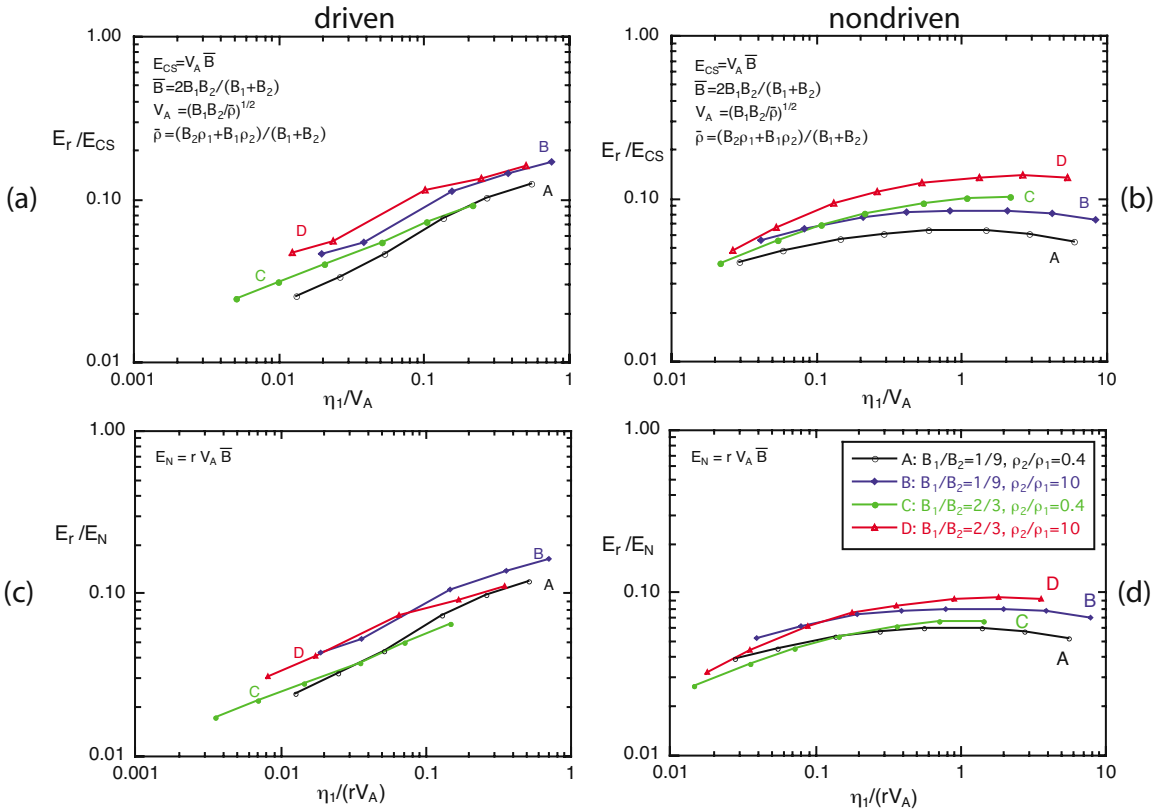

FIG. 4. (Color online) Maximum reconnection rates as function of resistivity for (left) driven and (right) nondriven cases defined in Table I. Different normalizations are indicated in the figure: the top panels [(a) and (b)] are based on the Cassak–Shay formula for the incompressible limit, while the reconnection rates in the bottom panels [(c) and (d)] are scaled by including the compression factor r given by Eq. (28).

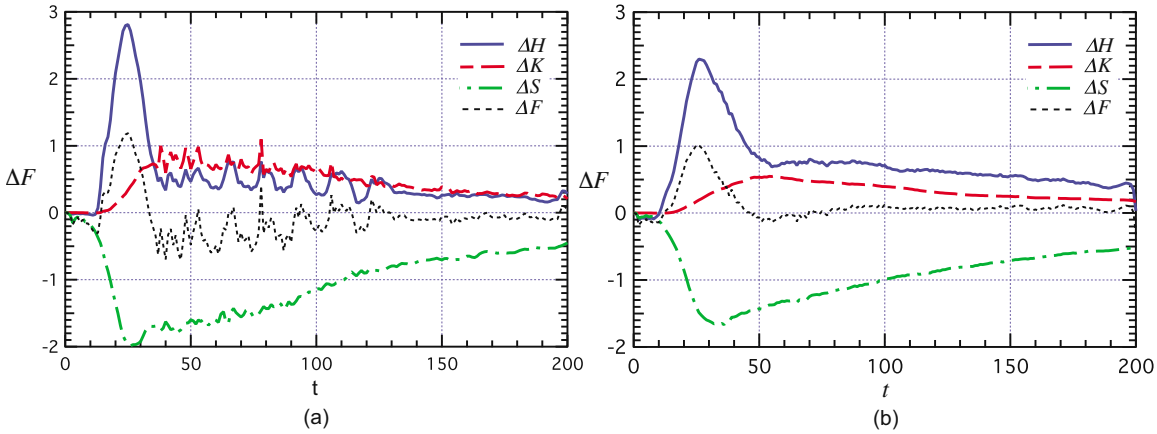

FIG. 5. (Color online) Energy transfer as function of time for nondriven symmetric cases with $\eta_1=1$ and $d_x=d_z=0.5$: (a) for $\beta=0.1$ and (b) for $\beta=1$. ΔH (solid lines), ΔK (dashed lines), and ΔS (dash-dotted lines) represent the differences between outgoing and incoming enthalpy flux, bulk kinetic energy flux, and Poynting flux, respectively, integrated over the boundaries of a box $0<x<10$ and $z<3$. The dotted lines represent the net energy flux ΔF into or out of the box.

magnetic fields and plasma beta but different density ratios, cannot be reduced by inclusion of the factor r.

As in Fig. 3(b), the normalization of the abscissa in Figs. 4(c) and 4(d) is based on the scaling for the Sweet–Parker regime of small resistivity given by Eq. (41) but the proper scaling at larger values of η is not *a priori* clear. We have tried to use abscissa values η/v_A instead of $\eta/(rv_A)$. However this tended to shift the locations of the maxima in E_r between the pairs A and B versus C and D away from each other. Thus keeping the same scaling as in the Sweet–Parker regime gave a better overall agreement.

IV. MHD SIMULATIONS: ENERGY TRANSFER AND CONVERSION

In this section, we investigate the energy conversion on the basis of the resistive MHD simulations, focusing on the nondriven cases. Figure 5 shows the differences between outgoing and incoming energy fluxes as function of time for two nondriven symmetric cases with $\eta_1=1$ and $d_x=d_z=0.5$, (a) for $\beta=0.1$, and (b) for $\beta=1$ in the inflow region. The fluxes are integrated over the boundaries of a (half)box $0<x<10$, $-3<z<3$. Solid lines correspond to the difference in enthalpy flux, ΔH, dashed lines to bulk kinetic energy, ΔK, and dash-dotted lines to the difference in Poynting flux, ΔS. Both cases show an initial burst of net enthalpy flux, which is not entirely balanced by incoming magnetic energy (Poynting) flux, as indicated by the dotted lines, which represent the total energy flux out of the box. At later times a more steady behavior is assumed with a balance of incoming and outgoing energy fluxes. For small β [Fig. 5(a)] the conversion to enthalpy and bulk kinetic energy flux is close to the predicted 1:1 ratio, while at larger β [Fig. 5(b)] the conversion to enthalpy flux dominates. The gradual decrease of the fluxes after the initial impulsive release stems from the fact that the magnetic field and the density in the inflow regions decrease slowly as reconnection proceeds. The normalization is based on the initial values of B_2 and ρ_1.

Figure 6 shows the evolution of the energy conversion for the four cases of asymmetric reconnection defined in Table I, using $\eta_1=0.1$ and $d_x=5$, $d_z=1$. ΔH (solid lines), ΔK (dashed lines), ΔS (dash-dotted lines), and ΔF (dotted lines) again represent the differences between outgoing and incoming enthalpy flux, bulk kinetic energy flux, Poynting flux, and total energy flux, respectively, integrated over the boundaries of a box $|z|<3$ and $0<x<12$ in cases A and B, $0<x<20$ in cases C and D. (The more elongated box size in cases C and D was chosen because of the somewhat slower evolution and the correspondingly lower aspect ratio of outflow to inflow width.) The fluxes are evaluated by accounting for the motion of the x-line. As in the symmetric cases (Fig. 5), all asymmetric simulations show an initial dominance of conversion to enthalpy flux, which is not completely balanced by the incoming Poynting flux, as evidenced by the net fluxes ΔF. Later the four cases exhibit quite different behavior in the energy conversion. Case C (lower left) with the weakest asymmetries ($B_1/B_2=2/3$, $\rho_2/\rho_1=0.4$) shows a behavior close to that of the symmetric case (Fig. 5). The incoming Poynting flux is fairly equally divided into enthalpy flux and bulk kinetic energy flux as predicted by our simple scaling estimates (Sec. II). Case D (lower right) with modest magnetic field asymmetry ($B_1/B_2=2/3$) but strong density ratio ($\rho_2/\rho_1=10$) behaves similarly, although more energy is converted into enthalpy flux.

Particularly cases A and B show sporadic strong variations in the transfer rates. These wiggles have been identified as fast mode waves launched by the initial burst of reconnection, propagating upstream and being reflected at the boundary. Apparently the subsequent reflection of the returning wave packets at the strong magnetic field and pressure gradients between the two inflow regions in cases A and B plays a role in their repeated occurrence. Their main effect appears to be the occasional modulation of the inflow speed, leading to the sporadic variation of the converted energy but they do not seem to have a significant effect on the overall reconnection rate and the energy budget.

The two cases with strong magnetic field asymmetry show initially low conversion to bulk kinetic energy but the

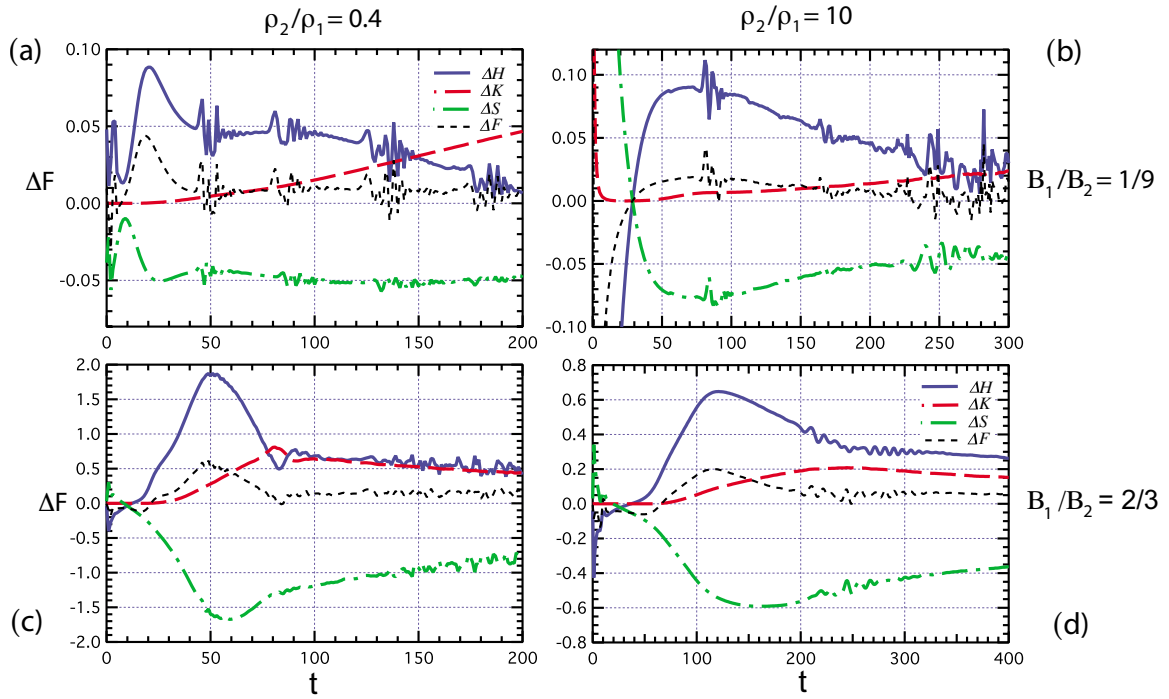

FIG. 6. (Color online) Energy transfer as function of time for four nondriven asymmetric cases A–D defined in Table I [corresponding to panels (a)–(d)] with $\eta_1=1$ and $d_x=d_z=0.5$. ΔH (solid lines), ΔK (dashed lines), and ΔS (dash-dotted lines) represent the differences between outgoing and incoming enthalpy flux, bulk kinetic energy flux, and Poynting flux, respectively, integrated over the boundaries of a box $|z|<3$ and $|x|<12$ in cases A and B, $|x|<20$ in cases C and D. The dotted lines represent the net energy flux ΔF into or out of the box.

rate increases in time, while the conversion to enthalpy flux decreases, so that at later times, the conversion to kinetic energy may dominate. We note, however, that the cases with strong magnetic field asymmetry are characterized by large plasma pressure on the low field side and hence large thermal energy inflow from this side, so that the total thermal energy outflow by far dominates also on the outflow side. The converted enthalpy flux thus is only a very small fraction of the total enthalpy flux through the system.

The pressure asymmetry plays a significant role also in the acceleration process. This is illustrated by Fig. 7 which shows the velocity components v_x, normalized by the predicted outflow speed v_o, Eq. (15), and the pressure p for cases A and C (Table I) at $t=200$ and $t=100$, respectively, together with magnetic field lines (black contours). The white rectangles indicate the box used for integration of the fluxes shown in Fig. 6. The heavy lines represent paths of fluid elements that end at $x=20$ in the region of fast outflow.

At first sight the outflows in the two cases appear similar. However, closer inspection shows that in case A (two top panels) the fast outflow is very strongly field-aligned and exceeds the predicted outflow speed v_o, whereas in case C (two bottom panels) there is a significant portion of the outflow perpendicular to the magnetic field and the outflow speed is very close to its predicted value. Also the pressure variation along the paths is different. Although the pressure distributions represent snapshots corresponding to the end points of the paths at $x=20$, whereas the paths represent a time sequence, they nevertheless illustrate that in case A the pressure decreases toward the end of the paths whereas in case C p increases during the early evolution but remains relatively unchanged during the acceleration stage.

The different effect of pressure gradients is demonstrated more quantitatively by Fig. 8, which shows the forces in the x direction as function of x for the two paths of cases A and C whose starting points are indicated by white dots in Fig. 7. Solid lines show the Lorentz force and dashed lines the pressure gradient force. In case C (bottom panel) the Lorentz force clearly dominates, as postulated in Sec. II, whereas in case A (top panel) both forces are relevant and the pressure force even dominates. This is despite the fact that the pressure distribution shown in Fig. 7 (second panel) appears to be nearly one-dimensional with $|\partial p/\partial x| \ll |\partial p/\partial z|$. The important role of the pressure gradient force in case A (and similarly in case B, not shown here) is related to the strong magnetic field asymmetry, which causes an offset between field and flow patterns[6,9] such that the fast outflow is predominantly on the high-field side and becomes very strongly field-aligned. In this case only pressure gradients may provide acceleration. The fact that in case A the final speed exceeds the predicted outflow speed by a factor of up to ~ 1.4 is consistent with conclusions of Ref. 20 of the effect of pressure gradients.

The excess conversion to enthalpy flux seen in Fig. 6(d) is due to an opposite effect of the pressure gradient force, which may balance, in part, the Lorentz force in the outflow region. (This is seen to a minor extent also in case C of Fig. 8 for $x<10$, however, this deceleration is compensated in that case by an acceleration from $\partial p/\partial x$ for $x>10$.) The deceleration leads to compressional heating and thereby a conversion from bulk kinetic to thermal energy flux.

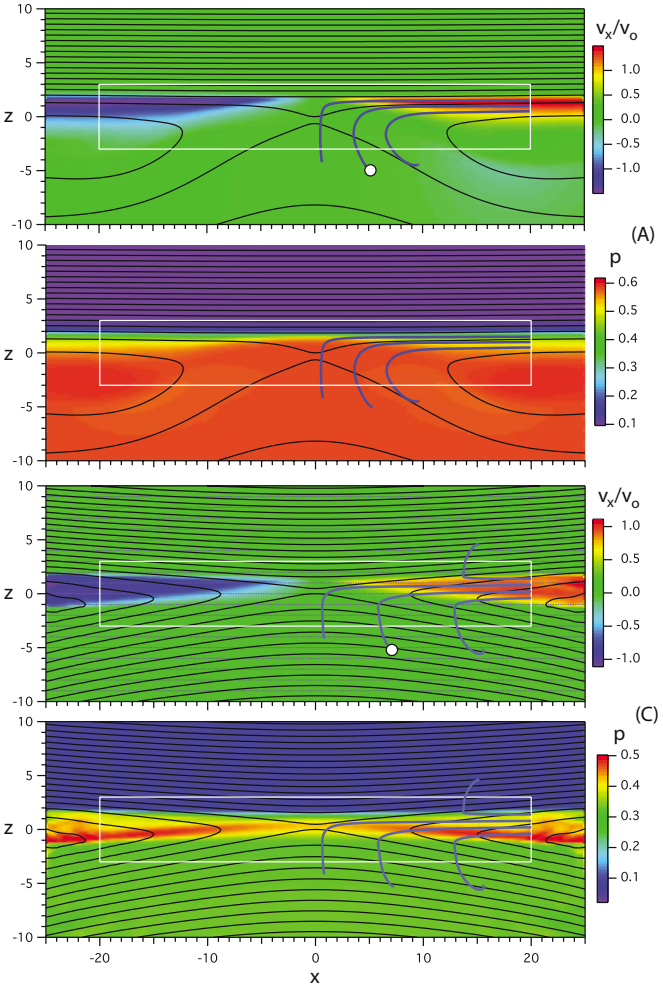

FIG. 7. (Color online) Snapshots of the velocity components v_x, normalized by the predicted outflow speed (15), and the pressure p for cases A and C (Table I) at $t=200$ and $t=100$, respectively. Black contours are magnetic field lines. The white rectangles indicate the box used for integration of the fluxes shown in Fig. 6. The heavy lines represent paths of fluid elements that end at $x=20$ in the region of fast outflow. White dots indicate the starting points of two orbits chosen for Fig. 8.

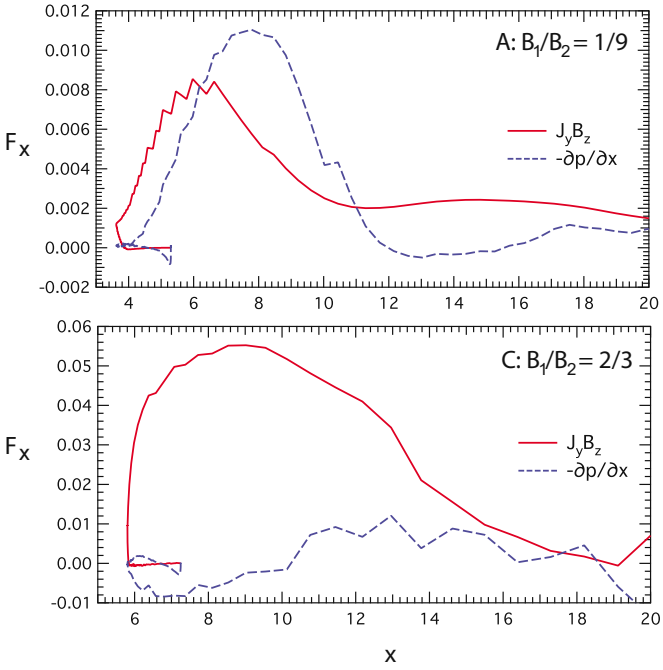

FIG. 8. (Color online) Forces in the x direction as function of x for two paths of cases A and C (Table I) indicated by white dots in Fig. 7, respectively. Solid lines show the Lorentz force and dashed lines the pressure gradient force.

V. SUMMARY AND CONCLUSIONS

Using simple balance arguments akin to those described by Priest and Forbes[20] for symmetric reconnection and Cassak and Shay,[6] Swisdak and Drake[21] for asymmetric steady reconnection, we have derived scaling laws for the reconnection rate, given by expression (25), which generalize previous results by including compressibility in addition to asymmetry between the plasmas and fields in the inflow regions. The reconnection rate obtained by Ref. 6 for the incompressible case is modified by a factor $r=\rho_o/\bar{\rho}$, which represents the compression ratio between the outflow density ρ_o and a density $\bar{\rho}$ corresponding to the simple mixing of the inflowing plasmas without compression. The factor r depends on the adiabatic index γ as well as on the plasma β and the magnetic field ratio between the two inflow regions but not on the densities. For $\gamma=5/3$, the compression factor r varies between 1 (for large β or large magnetic field ratio) and 2.5 (for small β). For symmetric reconnection the factor r becomes identical to the compression ratio derived by Soward and Priest.[22]

The main simplifying assumptions are as follows. (1) Neglect of gradients of external parameters along the reconnecting current sheet; this also implies that the effect of pressure gradients in the acceleration or deceleration along the sheet is neglected, such that the acceleration is assumed to result entirely from Lorentz forces; (2) neglect of the velocity components v_x in the inflow regions; (3) assuming that the magnetic field strength in the outflow region is small compared to the inflow fields; and (4) representation of the outflow plasma by single values of density, speed, pressure, and magnetic field perpendicular to the outflow direction. However, this latter assumption is generalized in the Appendix.

We also found that, under these assumptions, one half of the incoming total magnetic energy flux (Poynting flux) is converted to bulk kinetic energy while the other half is added to enthalpy flux, i.e., thermal energy. This result generalizes earlier findings (e.g., Ref. 20) to asymmetric and compressible scenarios.

Using resistive MHD simulations we then evaluated the scaling laws and the energy conversion for different symmetric and asymmetric scenarios. We found some improvement of the scaling of the reconnection rate over earlier scaling results based on the incompressible approximation. However, inclusion of the compressibility could not account for differences in cases that differed only by the density ratio but not in the magnetic fields and the plasma beta. Overall we also found that the conversion of incoming Poynting flux was split between bulk kinetic energy and enthalpy flux, although the 1/1 split predicted by the simplified model was

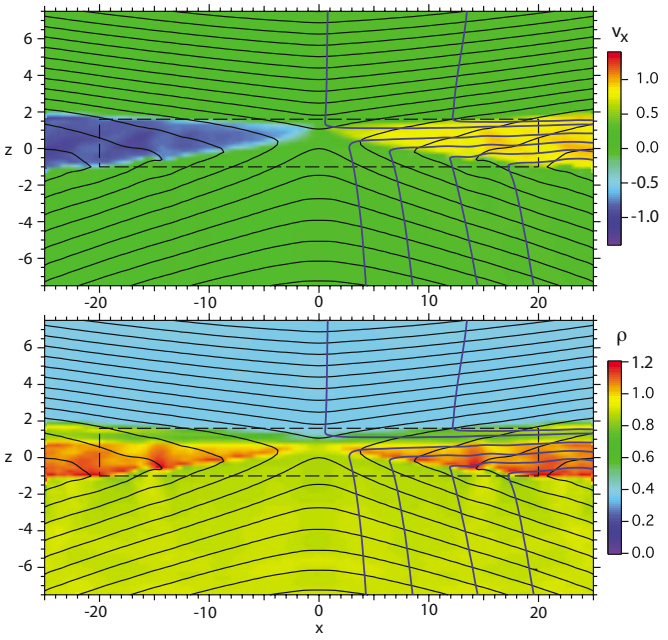

FIG. 9. (Color online) Velocity v_x (top) and density ρ (bottom) for case C in the x,z plane at $t=120$, using $\eta_1=0.1$, $d_x=1$, and $d_z=0.5$. Solid heavy lines in the right half of the figure indicate streamlines. The dashed rectangle indicates the width of the outflow region for a chosen half-length $L=20$.

found primarily for weak asymmetry and low plasma beta. In most cases the conversion to enthalpy flux dominated. This is largely due to pressure gradient forces along the outflow direction, which in part balance the Lorentz force and thereby slow down the flow and convert bulk kinetic energy to thermal energy by compressional heating.

Cases with strong magnetic field asymmetry further showed a significant temporal variation with increasing conversion to kinetic and decreasing conversion to enthalpy flux. To identify the reason for this different behavior, we investigated the acceleration of fluid elements that contribute to the fast outflow. We found that in these cases pressure gradients along the magnetic field in the outflow region, although weak, may nevertheless contribute significantly to the acceleration. In these strongly asymmetric cases the incoming plasma stems almost entirely from the low field, high pressure, region and is ejected into the higher field, lower pressure, side, with the velocity strongly aligned with the magnetic field. Accordingly, pressure gradients are needed to accelerate the plasma along the magnetic field.

ACKNOWLEDGMENTS

This work was performed under the auspices of the U.S. Department of Energy, supported by NASA's Heliophysics Theory and SR&T Programs, and through a grant from NASA's MMS/SMART program.

APPENDIX: NONUNIFORM OUTFLOW

In Sec. II, we have assumed that the outflow parameters ρ_o, v_o. p_o, and B_o are uniform over the width of the outflow region. Figure 9 demonstrates, for case C with modest asymmetries, that this assumption is reasonably well satisfied for

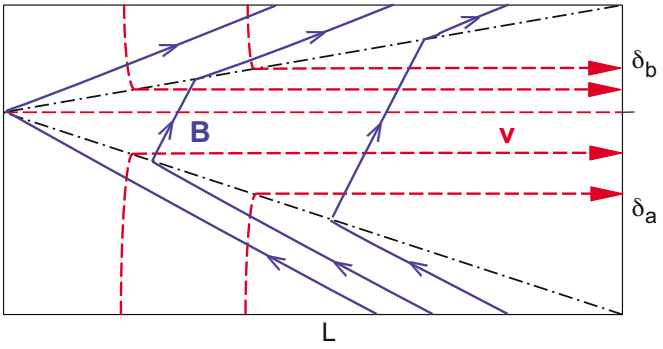

FIG. 10. (Color online) Schematic of the reconnection site including two outflow regions with the widths δ_a and δ_b, respectively. Solid lines represent magnetic field lines and dashed lines are streamlines. The dash-dotted lines separate inflow and outflow regions. The displacement between x-point and flow stagnation point, which is of the order of the size of the diffusion region is disregarded.

the outflow speed $v_o \approx v_{ox}$. The steady state condition (6) and pressure balance (9) then imply that the magnetic field component perpendicular to the outflow direction, $B_o=B_{oz}$, and the outflow pressure p_o are uniform as well. In contrast, the outflow density in Fig. 9 shows a clear demarcation between the plasmas originating from the two different sides. In principle, thermal conduction, which is not included in our simulations, could mix the two populations and reduce the density and temperature difference.[25,26] However, the net effect should involve a competition between outflow [at or near the hybrid Alfvén speed (2)] and the thermal conduction, which is expected to propagate at the thermal speed. A proper treatment would require PIC or hybrid simulations. Here we consider the modifications of the scaling derivations associated with a splitting of the outflow into two segments. The configuration demonstrated by Fig. 9 is schematically shown in Fig. 10. For simplicity, we also disregard the displacement between x-point and flow stagnation point, which is of the order of the size of the diffusion region, although this might be included as well (e.g., Refs. 6 and 26). That means we consider primarily Petschek type configurations, where most of the energy conversion takes place outside the diffusion region.

We now apply the conservation laws discussed in Sec. II to the modified scenario illustrated in Fig. 10. Solid lines represent magnetic field lines and dashed lines are streamlines. The dash-dotted lines separate inflow and outflow regions. (The balance arguments below do not necessarily require that these are sharp discontinuities, as indicated in Figs. 9 and 10.) Mass conservation (5) becomes modified to

$$L(\rho_1 v_1 + \rho_2 v_2) = (\delta_a \rho_a + \delta_b \rho_b) v_o. \tag{A1}$$

For the derivation of the outflow speed (15), we now use the force balance in a conservative form that is more in line with our use of the other conservation laws

$$\nabla \cdot \left(\rho \mathbf{v}\mathbf{v} + p_{\rm tot} \underline{\mathbf{I}} - \frac{1}{\mu_0} \mathbf{B}\mathbf{B} \right) = \mathbf{0}. \tag{A2}$$

Here $p_{\rm tot}$ is the sum of magnetic and plasma pressure as defined by Eq. (7). Integrating the x component of Eq. (A2)

over a finite box and conversion into a surface integral then leads to

$$\oint \rho v_x v_n ds = \frac{1}{\mu_0} \oint B_x B_n ds, \tag{A3}$$

where we have used that the total pressure is approximately constant over the box length L so that the surface integral vanishes. If the integrals in Eq. (A3) were taken over the entire box of Fig. 1 they would vanish for symmetry reasons. Hence we take the integrals only over half a box, $x>0$, as shown in Fig. 10. At the left boundary v_x vanishes for symmetry reasons, and at the upper and lower boundaries v_x is small by assumption. Therefore there is only a contribution to the integral of $v_x v_n$ from the right boundary, where $v_x=v_n=v_o$. At the top and bottom boundaries we find $B_x=B_2$ and $B_n=B_{z2}$ and $B_x=-B_1$ and $B_n=-B_{z1}$, respectively. At the right boundary, $B_x=B_n=B_{ox}$ and at the left boundary, $B_x=B_n\approx B_1$ for the lower portion and $B_x=-B_n\approx B_2$ for the upper portion. This leads to the balance

$$(\rho_a\delta_a+\rho_b\delta_b)v_o^2 \approx \frac{1}{\mu_0}[B_1B_{1z}L+B_2B_{2z}L-B_1^2\delta_a-B_2^2\delta_b + B_{ox}^2(\delta_a+\delta_b)]. \tag{A4}$$

Here B_{1z} and B_{2z} are suitable average values along the bottom and top boundaries in Fig. 10. These values can be estimated from $\nabla\cdot\mathbf{B}=0$, which yields

$$\oint B_n ds = 0. \tag{A5}$$

We take the integral in Eq. (A5) separately over the upper and lower portions of the box in Fig. 10 and obtain

$$-B_{1z}L+B_{ox}\delta_a+B_oL+B_1\delta_a=0, \tag{A6}$$

$$B_{2z}L-B_{ox}\delta_b-B_oL+B_2\delta_b=0. \tag{A7}$$

The terms with B_{ox} in Eqs. (A6) and (A7) are smaller than the other terms by a factor ϵ and are therefore neglected. If B_{1z} and B_{2z} are then inserted into Eq. (A4), we obtain

$$(\delta_a\rho_a+\delta_b\rho_b)v_o^2=\frac{1}{\mu_0}B_o(B_1+B_2)L. \tag{A8}$$

We can now use Eqs. (A1) and (6) to obtain the outflow speed identical to Eq. (15)

$$v_o^2=\frac{B_1B_2}{\mu_0\bar{\rho}}. \tag{A9}$$

This result was already noted, without proof, by Ref. 26.

The evaluation of the energy balance becomes identical to that in Sec. II if we introduce an average outflow density defined by

$$\rho_o=\frac{\rho_a\delta_a+\rho_b\delta_b}{\delta_a+\delta_b}. \tag{A10}$$

This derivation is therefore not repeated here. The consequence is that the scaling of the reconnection rate and the compression factor $r=\rho_o/\bar{\rho}$ remain unchanged if ρ_o is defined by Eq. (A10).

[1] M. Øieroset, T. D. Phan, and M. Fujimoto, Geophys. Res. Lett. **31**, L12801, doi:10.1029/2004GL019958 (2004).
[2] J. T. Gosling, M. F. Thomsen, S. J. Bame, R. C. Elphic, and C. T. Russell, J. Geophys. Res. **95**, 8073, doi:10.1029/JA095iA06p08073 (1990).
[3] J. Heyvaerts, E. Priest, and D. M. Rust, Sol. Phys. **53**, 255 (1977).
[4] B. Schmieder, D. M. Rust, M. K. Georgoulis, P. Démoulin, and P. N. Bernasconi, Astrophys. J. **601**, 530 (2004).
[5] H. Isobe, T. Miyagoshi, K. Shibata, T. Yokoyama, and R. Matsumoto, Journal of the Earth Simulator **7**, 3 (2007).
[6] P. A. Cassak and M. A. Shay, Phys. Plasmas **14**, 102114 (2007).
[7] J. E. Borovsky and M. Hesse, Phys. Plasmas **14**, 102309 (2007).
[8] J. E. Borovsky, M. Hesse, J. Birn, and M. M. Kuznetsova, J. Geophys. Res. **113**, A07210, doi:10.1029/2007JA012645 (2008).
[9] J. Birn, J. E. Borovsky, and M. Hesse, Phys. Plasmas **15**, 032101 (2008).
[10] P. A. Sweet, Nuovo Cimento **8**, 188 (1958).
[11] E. N. Parker, J. Geophys. Res. **62**, 509, doi:10.1029/JZ062i004p00509 (1957).
[12] H. E. Petschek, in *AAS/NASA Symposium on the Physics of Solar Flares*, edited by W. N. Hess (NASA SP-50, Washington, DC, 1964), pp. 425–439.
[13] V. M. Vasyliūnas, Rev. Geophys. Space Phys. **13**, 303, doi:10.1029/RG013i001p00303 (1975).
[14] J. Birn, J. F. Drake, M. A. Shay, B. N. Rogers, R. E. Denton, M. Hesse, M. Kuznetsova, Z. W. Ma, A. Bhattacharjee, A. Otto, and P. L. Pritchett, J. Geophys. Res. **106**, 3715, doi:10.1029/1999JA900449 (2001).
[15] J. Birn, K. Galsgaard, M. Hesse, M. Hoshino, J. Huba, G. Lapenta, P. L. Pritchett, K. Schindler, L. Yin, J. Büchner, T. Neukirch, and E. R. Priest, Geophys. Res. Lett. **32**, L06105, doi:10.1029/2004GL022058 (2005).
[16] P. A. Cassak and M. A. Shay, Geophys. Res. Lett. **35**, L19102, doi:10.1029/2008GL035268 (2008).
[17] G. Paschmann, I. Papamastorakis, W. Baumjohann, N. Sckopke, C. W. Carlson, B. U. O. Sonnerup, and H. Lühr, J. Geophys. Res. **91**, 11099, doi:10.1029/JA091iA10p11099 (1986).
[18] D. Q. Ding, L. C. Lee, and C. F. Kennel, J. Geophys. Res. **97**, 8257, doi:10.1029/92JA00431 (1992).
[19] P. L. Pritchett, J. Geophys. Res. **113**, A06210, doi:10.1029/2007JA012930 (2008).
[20] E. R. Priest and T. G. Forbes, *Magnetic Reconnection: MHD Theory and Applications* (Cambridge University Press, Cambridge, England, 2000).
[21] M. Swisdak and J. F. Drake, Geophys. Res. Lett. **34**, L11106, doi:10.1029/2007GL029815 (2007).
[22] A. M. Soward and E. R. Priest, J. Plasma Phys. **28**, 335 (1982).
[23] J. Birn and M. Hesse, J. Geophys. Res. **106**, 3737, doi:10.1029/1999JA001001 (2001).
[24] A. Otto, J. Geophys. Res. **106**, 3751, doi:10.1029/1999JA001005 (2001).
[25] M. Nakamura and M. Scholer, J. Geophys. Res. **105**, 23197 (2000).
[26] P. A. Cassak and M. A. Shay, Phys. Plasmas **16**, 055704 (2009).